Structural and Magnetic Analysis of Magnesium-Iron Oxide Nanoparticles Produced by Sol-Gel Auto-Combustion

Zahraa Jabbar Hamakhan, Fatma Yaseen Mohamed, Rudainah Sedeeq Abdul Sttar and Jasim Mohamed Al-Khalidi
Department of Physics, College of Science, University of Diyala, 32001 Baqubah, Iraq
{zahraa.jabbar, Fatimayaseen, rudainahsadeeq, jasim_mo}@uodiyala.edu.iq

Keywords: Magnesium Ferrite, Sol-Gel Auto Combustion Method, XRD, FESEM, VSM, Superparamagnetic Behavior.

Abstract: The research examines the impact of various temperatures on the micro and nano structures in addition to the magnetic characteristics of MgFe2O4 spinel ferrite that was produced by the sol-gel auto-ignition process. The temperatures tested were 250℃ (as burnt), 600, 700, 800, and 900 °C. The produced ferrite's structure and magnetic characteristics were investigated using X-ray diffraction (XRD), Field Emission Scanning Electron Microscope (FESEM), and vibrating sample magnetometer (VSM). According to XRD patterns, the produced system contains a cubic phase of spinel MgFe2O4, belonging to the space group Fd3m. Depending on Tc, the crystallite sizes grew in the range of (33.438-58.715) nm when the calcination temperature rose. Then , the calculated lattice parameters are a= (8.364, 8.387, 8.374, 8.381, and 8.381 Å) at Tc=as burnt, 600, 700, 800, and 900 °C, respectively. However, the mean strain values decreased from 3.646 to 2.070. Also, dislocation density (δ) decreased with increasing temperature from 8.943 to 2.900 nm-2. Analysis using FESEM reported that the average grain size of all the calcined samples increased with increasing calcination temperature with an average grain size around (59.426-128.254) nm. Elemental analysis using energy-dispersive X-ray spectroscopy has also shown that all samples include Mg, Fe, and O. At ambient temperature, VSM detected a significant proportion of superparamagnetic particles; samples calcined at 800 °C and 900 °C exhibited pure superparamagnetic behavior with Hc=0, saturation magnetization's value decreased from 24.862 to 23.834 emu/g when increasing temperature from 250 to 600◦C, after that increased at other temperatures. Remnant magnetization increased with increasing calcination temperature in the range of (0.026-5.181)emu/g.

1 INTRODUCTION

Ferrite magnetic materials offer benefits compared to bulk ferrite materials, including significantly reduced size and an increased surface area to volume ratio [1]. Spinel ferrite crystals MFe2O4 (M = Mg), constitute a significant category of magnetic materials. They exhibit notable properties, including a low melting point and low magnetic transition temperature, in addition to high specific heat and huge expansion coefficient [2]. Due to the above properties, ferrite materials find extensive application in ferrofluid field, magnetic pigments and information storage [2]. Their magnetic properties and molecular-level responsiveness make these materials suitable for various biomedical applications, such as targeted drug delivery, diagnostics, and magnetic separation [2]-[4]. Moreover, they are being explored as potential alternatives to conventional contrast agents in magnetic resonance imaging (MRI) [5]. Through linking with tetrahedral (A-sites) and octahedral (B-sites), the crystal structure of spinel material features a cubic close packing of O-2 ions [6]. MgFe2O4 is a significant magnetic material characterised by a cubic spinel ferrite structure with normal type and functioning as a soft magnetic semiconductor [7]. Magnesium ferrite employed in high-density recording media [8], heterogeneous catalysis [9], and sensors [10], among other applications. Magnesium ferrite exhibits a notable photoelectric effect [11] and is considered as a likely applicant for localised heating system in cancer treatment for human [12]. Due to the preparation method greatly influence on the physical characteristics of spinel ferrite material, multiple techniques engaged to synthesise MgFe2O4, including precipitation methods [13],

microemulsion [14], sonochemical processes [15], sol-gel [16], hydrothermal approaches [17] and etc. Each of these processes presents distinct advantages and disadvantages, contingent upon the desired properties and applications. A recent development in synthesis and processing techniques is the sol-gel auto-ignition Process which recognized for its easiness and versatility. This method is significant to produce high quality ceramics, including both structural and functional types, as well as catalysts, composites, and spinel structured ferrite [18], [19]. This research aims to synthesis crystalline magnesium ferrite by sol-gel auto-ignition Process at varying calcination temperature and to examine its structural and magnetic characteristics through XRD, FESEM, and VSM analysis.

2 EXPERIMENTAL

2.1 Basic Materials

The materials which use through the study included iron nitrate nonahydrate (Fe(NO3)3.9H2O, Central Drug House (CDH), 98%), magnesium nitrate (Mg(NO3)2.6H2O, Himedia, 98%), ammonium hydroxide (NH4OH, Central Drug House(CDH), 35%) and citric acid (C6H8O7.H2O, Alpha Chemika, 99.5%). All experiments utilised distilled water (DW).

2.2 Preparation Technique

$MgFe_2O_4$ produced using defined sol-gel auto-ignition Process [18], [19]. In a standard procedure, solutions containing specified amounts of Iron (III) nitrate and magnesium nitrate were formulated using 200 ml of distilled water as the dissolving medium. Metal nitrates were mixed with an Mg:Fe stoichiometric ratio of 1:2, and citric acid was added at a 1:1 molar ratio to prepare aqueous solution. The pH of the final solution was precisely controlled and set to 7 by the gradual addition of ammonia, resulting in a green colouration solution. Then, the solution was heated to approximately 80°C and gradually evaporated by hot plate with agitation until it reached a highly viscous state. After that, raising the temperature of the hot plate to 250°C for 30 sec, resulting in the gel undergoing self-propagating combustion, which produced a loose powder. The powder was placed in the oven for drying at 110ºC for 30 minutes. The powder was subsequently calcined in air at various temperatures (600, 700, 800, and 900°C) for two hours, yielding pure spinel magnesium ferrite. Figure 1 presents the typical images of prepared sample. A fine powder exhibiting the characteristic brown colour of $MgFe_2O_4$ was produced.

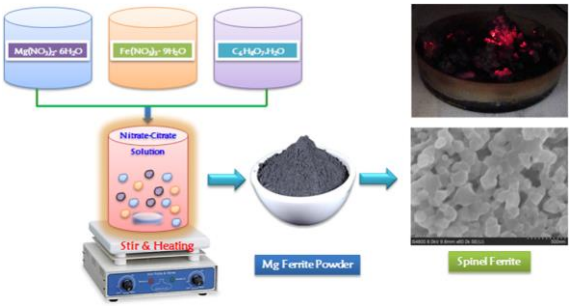

Figure 1: Flow diagram for sol-gel auto-ignition process to synthesis $MgFe_2O_4$ spinel ferrite.

2.3 Characterizations

Structural properties, including crystallinity and phase investigation of the produced products was performed using XRD system with a Shimadzu diffractometer (XRD-6000) employing a Cu-Kα monochromatic source (λ=1.5406 Å). The analysis covered the 2θ range between 20° and 80° at a scan speed of 8.0000 degrees per minute. The surface morphology and grain dimensions were investigated via Field Emission Scanning Electron Microscopy (FESEM-MIRA3-Iranian origin). A vibrating sample magneto- meter (VSM-LBKFB- Iranian origin) was used to determine the magnetization measurements were conducted on ferrite samples with an applied field of up to 15 kOe at room temperature.

3 RESULTS AND DISCUSSIONS

3.1 The XRD Result

Figure 2 shows the XRD forms of magnesium ferrite powders that were as-burned and calcined at different air temperatures for 2 hours. The creation of a single spinal phase with space group Fd3m was verified by the detected planes (311), (220), (422), and (511), which are associated to spinel cubic structure. Peaks in XRD patterns of the calcined samples became sharper and more intense with increasing calcination temperature, suggesting that the crystalline quality improves with increasing calcination temperature [2]. The ICSD Card No.01-073-2211, which is a standard diffraction line of magnesium ferrite, was used to compare all of the diffraction peaks. These findings corroborate those of earlier research [7], [20]. The XRD results demonstration that the sol-gel auto-

ignition process is capable of producing pure crystalline MgFe2O4 ferrite. To get a better understanding of the crystal structure, a number of structural parameters were computed from the XRD data and compared with several theoretic models. These parameters included crystallite size, lattice constant, XRD density, bond lengths, strain, and dislocation density (Table 1).

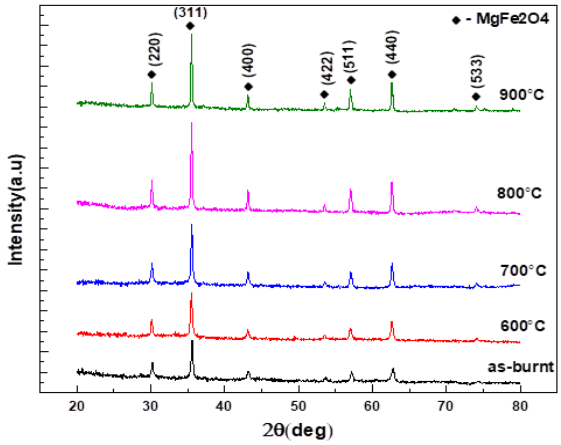

Figure 2: XRD pattern of $MgFe_2O_4$ nanoparticles at as burnt and different calcination temperatures (600, 700, 800, 900) ℃ for 2 hours.

Scherer's equation was used to calculate the crystallite size (D) of the samples by using the FWHM of the high intensity peak (311) [21], [22].

$$D = \frac{K\lambda}{\beta \cos\theta}. \quad (1)$$

The relation indicated below [23], [24] was used to calculate the lattice parameter (a), XRD density (ρ_x), hopping lengths L_A (A-site), and L_B (B-site).

$$a = d_{hkl}\sqrt{h^2 + k^2 + l^2}, \quad (2)$$

$$p_x = \frac{8M}{Na^3}, \quad (3)$$

$$L_A = 0.25a\sqrt{3}, \quad (4)$$

$$L_B = 0.25a\sqrt{2}. \quad (5)$$

The structural properties of ferrite nanoparticles were studied by calculating the average strain (ε) values using the Stokes-Wilson equation [25], [26]:

$$\varepsilon = \left(\frac{\beta}{4}\right) \tan\theta. \quad (6)$$

In addition, to get the dislocation density δ, use the equation [27]:

$$\delta = \frac{1}{D^2}. \quad (7)$$

In this equation, D stands for crystallite size, K for Scherer coefficient and is equal to 0.89 for spherical crystallite shape, λ is x-ray's wavelength, θ for Bragg's angle, β is the full width for half maximum (FWHM), M is the molecular weight of the sample, N is Avogadro's number, plus d_{hkl} represents the interplanar distance of each plane characterised by Miller indices (hkl). The larger crystallite sizes seen in Figure 3a are likely the result of a greater growth rate at higher calcination temperatures. Holds true in line with previous research [28]. The burned powder showed that wide peaks in the XRD forms suggesting that ferrite nanoparticle's crystal structure did not expand as much. But, growth of grains in the ferrite particles may explain why the peaks became sharper and more intense when the calcination temperature was increased Figure 2 [29].

The experimental value of the lattice parameter at different calcination temperatures is consistent with the theoretical values reported in the standard ICSD Card. It seems that cations are migrating back to their initial lattice positions, as the value of the lattice parameters (a) growth from 8.364 to 8.387 Å with the calcination temperature increased from as burnt (250°C) to 600°C. After that, the value decreased to 8.374 Å with increasing Tc to 700°C, then, it stabilizes at 8.381 Å at 800 and 900°C. These results are approximately consistent with reference [7]. Figure 3a shows the temperature variation during calcination relative to the lattice constant and crystallite size. The values of the XRD density (ρ_x) increase and decrease once depending on the lattice parameters with temperature, as is known, since the relationship between the two is inversely proportional. The shifts in the lattice parameters might explain the values and little fluctuation of the hopping distances L_A and L_B with rising calcination temperatures [30]. As the calcination temperature rises, the strain falls, eventually reaching a minimum at very high temperatures. The high crystallite size (D) and lack of impurity phases during nanoparticle formation contribute to their minimum strain, which in turn explains this phenomenon [31]. The dislocation density values dropped as the calcination temperature rose, reaching a low between 8.943-2.900 nm^{-2} at higher temperatures [32]. A crystal's dislocation density, measured in units of volume/length, is an indicator of the number of crystal defects. All of the manufactured samples have excellent crystalline characteristics, as stated before, and the low dislocation density figures prove it [31]. Table 1 and Figure 3b describe the estimated strain (ε) and dissociation density (δ) values for $MgFe_2O_4$ nanoparticles.

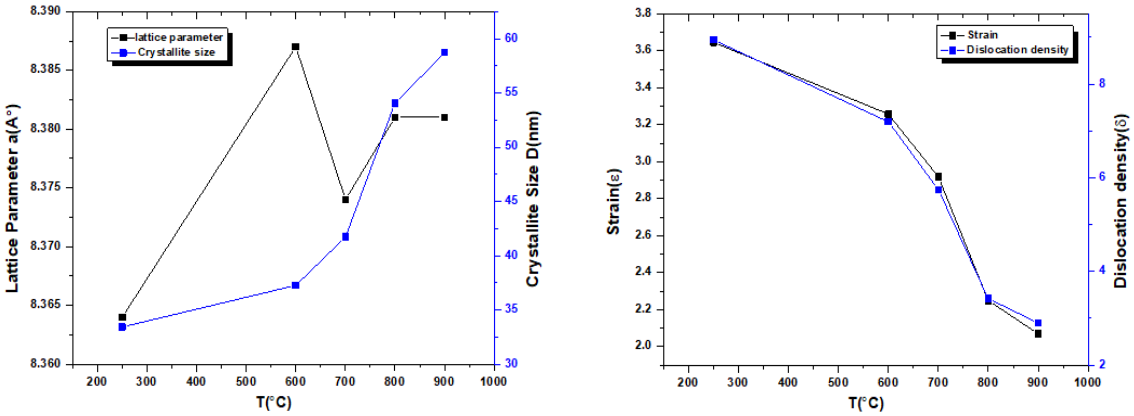

Figure 3: Variation of calcination temperature as a function of a) lattice parameters and crystallite size, b) strain and dislocation density.

Table 1: Crystallite size (D), lattice parameters (a), XRD density (ρ_x), hopping length (L_A) and (L_B), strain (ε), and dislocation density (δ) for $MgFe_2O_4$ nanoparticles that were manufactured both as-burnt and at various calcination temperatures.

Temp.°C	D_{XRD} (nm)	$D_{FE\text{-}SEM}$ (nm)	a(Å)	ρ_x(g/cm^3)	L_A(Å)	L_B(Å)	$\varepsilon \times 10^{-3}$	δ (nm^{-2})×10^{-3}
as-burnt	33.438	59.426	8.364	4.542	3.621	2.957	3.646	8.943
600	37.276	67.272	8.387	4.505	3.631	2.965	3.258	7.196
700	41.723	77.460	8.374	4.526	3.626	2.960	2.917	5.744
800	54.080	104.908	8.381	4.514	3.629	2.963	2.249	3.419
900	58.715	128.254	8.381	4.514	3.629	2.963	2.070	2.900

3.2 FESEM

Figure 4a–e presents the field emission scanning electron microscopy (FESEM) images of magnesium ferrite ($MgFe_2O_4$) samples, including the as-burnt precursor and those calcined at 600, 700, 800, and 900 °C for 2 hours. These images illustrate the surface morphology, grain size, and shape of the synthesized material. The average grain size was calculated using ImageJ software (version 1.51j8).

All calcined samples exhibit nearly spherical grains, with particle size increasing as the calcination temperature rises [2], [30], [33]. The nanosized ferrite samples obtained in the as-burnt state and at 600 °C and 700 °C show average grain sizes of approximately 59.426 nm, 67.272 nm, and 77.460 nm, respectively [33]. These samples display irregular morphology, non-uniform size distribution, noticeable agglomeration, and slight porosity.

In contrast, more homogeneous and well-defined grains with average sizes of 104.908 nm and 128.254 nm are observed at 800 °C and 900 °C, respectively (Fig. 4d, e). These results indicate that the crystallization and development of the spinel structure of $MgFe_2O_4$ are significantly enhanced with increasing calcination temperature. Temperature plays a crucial role in determining both the size and morphology of the particles. As shown in Fig. 4d and e, a more uniform particle size distribution is achieved at higher temperatures.

The grain size distribution for each sample was analyzed using histograms, and the mean grain size (D_FESEM) was calculated using the following equation [34], [35]:

$$p(d) = \frac{1}{d\sigma_d\sqrt{2\pi}} \exp \frac{-1}{\sigma_d^2} \ln \left(\frac{d}{D_{\text{FESEM}}}\right). \quad (8)$$

Here, p(d) represents the probability density function of grain size, D_FESEM is the mean grain size, and σ_d is the standard deviation.

The absence of pores and voids in the synthesized samples may be attributed to the highly exothermic combustion reaction, which releases a large volume of gases during the synthesis process [25]. Table 1 presents the calculated D_FESEM values, while Figure 4 shows the corresponding grain size distribution histograms. The grain sizes obtained from FESEM are larger than those calculated from XRD analysis. This difference can be explained by the fact that ferrite nanoparticles may exhibit a multi-domain structure, where each grain consists of several crystallites with different orientations [36]. The increase in grain size with rising calcination temperature suggests that adjacent particles tend to fuse, leading to grain growth due to surface melting.

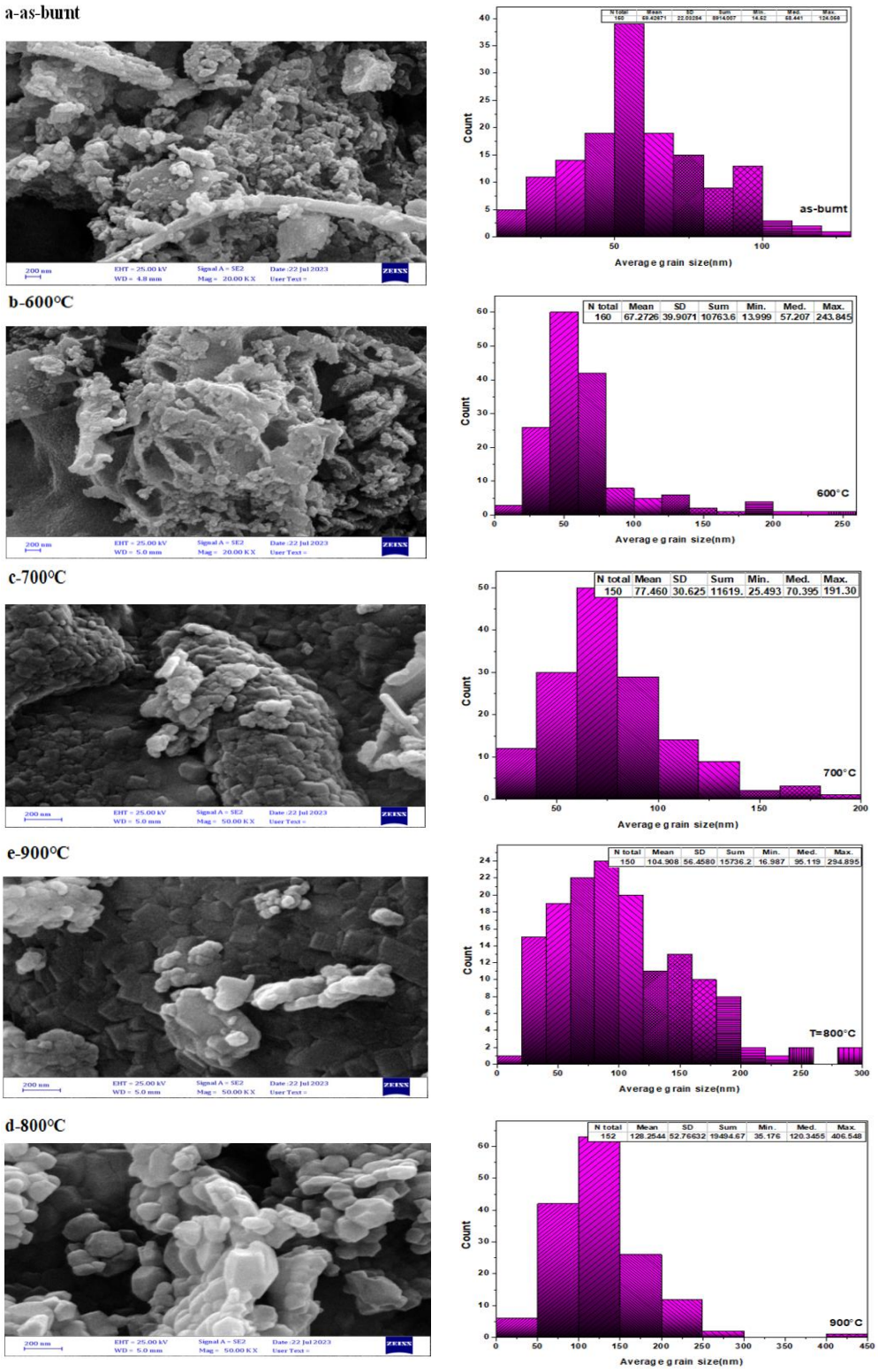

Figure 4: FESEM images and histogram of grain size for $MgFe_2O_4$ at as burnt and different temperatures (600, 700, 800, 900°C).

Energy-dispersive X-ray (EDX) analysis coupled with FESEM was used to confirm the elemental composition of the ferrite nanoparticles. Figure 5 shows the EDX spectra of the samples in the as-burnt state and after calcination at different temperatures (600–900 °C). The qualitative analysis confirms the presence of Mg, Fe, and O elements without detectable impurities. The results indicate that all samples are chemically homogeneous and that the $MgFe_2O_4$ phase with a spinel structure is successfully formed [33], with only a minor presence of Au due to sample coating.

3.3 VSM Study

The hysteresis loop of $MgFe_2O_4$ ferrites is presented in Figure 6, within ranges of ±15 kOe applied magnetic field at ambient temperature, at burned and different calcination temperatures (from 600 to 900°C). Anisotropy (K), coercive force (Hc), magnetic bohr (n_B), remnant magnetisation (Mr), saturation magnetisation (Ms), and remnant to saturation magnetisation (Mr/Ms) are shown in Table 2. Here are the formulae that may be used to determine these parameters [37]:

$$n_B = \frac{Mw \times Ms}{5585}, \quad (9)$$

$$H_c = \frac{0.96 \times K}{M_S}, \quad (10)$$

$$S = \frac{M_r}{M_s}. \quad (11)$$

The formula uses the sample's relative molecular mass, denoted as M_w. At Tc= 250°C (as burned), 600, 700, 800, and 900°C, the saturation magnetisation (Ms) values that were obtained are 24.862, 23.834, 30.409, 40.449, and 42.423emu/g, respectively. From as burned to 600°C, Ms drops marginally as Tc rises, but it rises sharply at all other calcination temperatures. While these numbers are greater than those that have been reported [33], they are rather near to those in Ref [7]. The main factor affecting on the saturation magnetisation is the Combining between the lattice parameters with the imperfect ordering of the cations between the octahedral and tetrahedral sites in the spinel lattice. In fact, by calcinating Mg-Fe (III) covered with double hydroxide inserted by hexacyanoferrate (III) ions at a little higher temperature of 1100 °C, Meng et al. [38] produced $MgFe_2O_4$ with high value of saturation magnetisation about 30 emu/g. Developments in the crystal structure, cation rearrangement, and magnetic ordering may also explain why the saturation magnetisation (Ms) of $MgFe_2O_4$ increases with increasing calcination temperature [39], [40]. Controlled synthesis and calcination procedures enable tweaking of magnetic characteristics to suit particular application needs by adjusting the cation distribution [41]. Calcination temperature has a clear impact on the the size and crystallinity of the crystals. Consequently, the nanocrystalline material's magnetic domains enlarge. By better aligning atomic spins in the applied magnetic field, the saturation magnetisation is enhanced as the crystal size increases [42]. Beyond that, in the range of (0.026-5.181) emu/g, Mr rises as the calcination temperature increases. An considerable percentage of superparamagnetic particles is present, as these low Mr/Ms ratios suggest [43]. According to the findings for $MgFe_2O_4$ nanoparticles described in References [44], [45], the ratio of Mr to Ms increases as the temperature increases. All of the synthetic samples had squareness ratio values lower than 0.5, which is consistent with magnetostatic interactions between the particles [29], [46]. At room temperature, Hc declined with increasing calcination temperature and have pure superparamagnetic behaviour appeared for samples calcined at 800 and 900 °C when Hc approaches zero. There was a linear relationship between the calcination temperatures and the coercivity. The number of domain walls rise when the crystallite size growth and the energy required to induce magnetisation by moving the walls of the domains decreases. It is anticipated that when the calcination temperature increases, the coercivity values would decrease because to the larger magnetisation produced by wall movement compared to single-domain rotation [47]. Anisotropy decreased with increasing in calcination temperature and decreased in coercivity values, according to research by Abdallah et al. [48]. Figure 7a, b shows the relationship between saturation magnetisation and coercivity according to calcination temperature and grain sizes. Anisotropy is constant, which quantifies the energy needed to rotate the magnetic moment away from the axis of magnetisation, is intimately related to a material's coercivity [49]. Coercivity (Hc) is often exactly proportionate to anisotropy (K), particularly in materials with a single magnetic domain [39]. Coercivity (Hc) drops as a consequence of magnetic domain reorientation made possible by a drop in anisotropy as temperatures rise [50]. The soft magnetic applications, such as transformers, inductors, and magnetic cores, benefit greatly from this property of these materials [51]. These results focus the importance of calcination temperature optimisation to modify the magnetic characteristics of

ferrite nano-particles for targeted applications, such as sensors, catalysis, and biomedicine [52]. The Bohr magnetic moment, which may be anywhere from 0.890 to 1.519 μ_B, is strongly related to the saturation magnetisation [51]. A significant dependence of the magnetic properties on the calcination temperature is very evident. Justification for this fact may be found in the relationship between temperature, crystallite size, cations distribution and lattice parameter as discussed before.

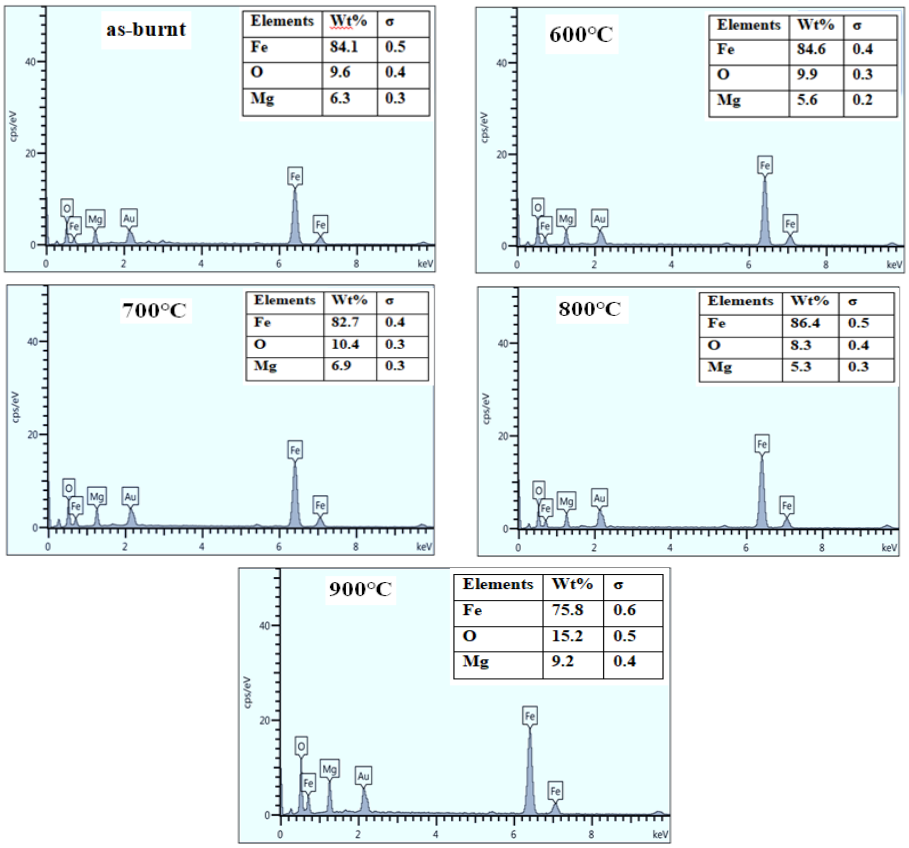

Figure 5: The EDX spectra for the $MgFe_2O_4$ ferrite at various calcination temperature.

Table 2: Magnetic characteristics of spinel Magnesium ferrite ($MgFe_2O_4$) at various temperatures.

Temp.°C	Ms (emu/g)	Mr (emu/g)	Hc (Oe)	Mr/Ms	n_B (μ_B)	$K \times 10^{-3}$ $(emu.Oe/g)$
as-burnt	24.862	0.026	128.087	0.001	0.890	3.317
600	23.834	1.053	56.038	0.044	0.853	1.391
700	30.409	1.799	24.016	0.059	1.088	0.760
800	40.449	2.249	0	0.055	1.448	0
900	42.423	5.181	0	0.122	1.519	0

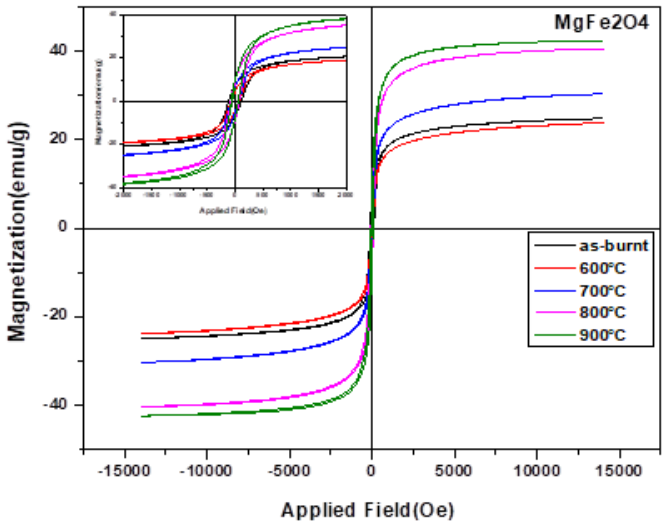

Figure 6: Hysteresis loop for $MgFe_2O_4$ spinel ferrite at as burnt and different temperatures (600, 700, 800, 900) °C.

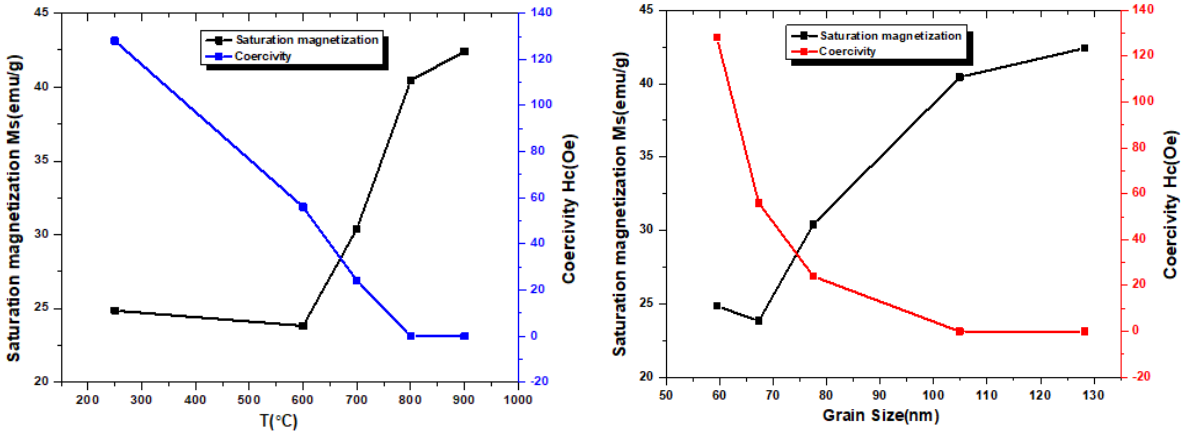

Figure 7: Saturation magnetization and coercivity as a function of a) calcination temperature and b) grain size.

4 CONCLUSIONS

This work used the sol-gel auto-ignition process to effectively synthesise $MgFe_2O_4$ ferrites. The behavior of the structural and magnetic characteristics of these ferrites were examined in relation to the impacts of calcination temperature. Calcination temperature has a clear effect on the size and crystallinity. By analysing the X-ray spectra, a pure cubic spinel phase structure has been revealed with average crystallite size increased with increasing calcination temperature. All of the experimental values of the lattice parameter at varies calcination temperatures are consistent with the theoretical values reported in the standard Card. Nano crystallites were observed in the FESEM images of the samples calcined at as burnt (250°C), 600, and 700 °C, with average grain sizes of 59.426, 67.272, and 77.460 nm, respectively. But, become out of the nano range with increasing calcination temperature to 800 and 900 °C to become 104.908 and 128.254 nm respectively. And the values of grain sizes obtained from FESEM images larger than those obtained from XRD data. FESEM exhibit highly agglomerated, nearly sphere-shaped. While verifying their spinel-like crystalline structure. EDX analysis verifies the elemental composition of the ferrite nanoparticles at all temperatures. VSM analysis shows that the samples which calcined at high temperatures of 800 and 900 °C, revealed superparamagnetic behaviour at ambient temperature (Hc = 0). By raising the calcination temperature to 800 and 900°C for 2 hours, respectively, good saturation magnetisation (Ms= 40.449 and 42.423 emu/g) was obtained. Mr and the ratios of Mr to Ms rise as the calcination temperature increases, except the values of squareness ratio at 800°C decreased

with increasing temperature from 700 to 800°C. All of the synthetic samples had squareness ratio values lower than 0.5. Anisotropy decreased with increasing calcination temperatures and becomes 0 at 800 and 900°C. And due to their structural and magnetic characteristics in addition to their advantageous grain size, MgFe2O4 nanoparticles have been identified for the MRI contrast agent.

REFERENCES

[1] I. Safarik and M. Safarikova, "Magnetic nanoparticles and bioscience," in Nanostructured Materials, H. Hofmann, Z. Rahman, and U. Schubert, Eds. Wien, Austria: Springer-Verlag, 2002, pp. 1–23.

[2] Sh. Kh. Durrani, S. Naz, M. Mehmood, M. Nadeem, and M. Siddique, "Structural, impedance and Mössbauer studies of magnesium ferrite synthesized via sol–gel auto-combustion process," J. Saudi Chem. Soc., vol. 21, pp. 899–910, 2017.

[3] C. Sun, J. S. H. Lee, and M. Zhang, "Magnetic nanoparticles in MR imaging and drug delivery," Adv. Drug Deliv. Rev., vol. 60, pp. 1252–1265, 2008.

[4] N. L. Rosi and C. A. Mirkin, "Nanostructures in biodiagnostics," Chem. Rev., vol. 105, pp. 1547–1562, 2005.

[5] J. H. Lee et al., "Artificially engineered magnetic nanoparticles for ultra-sensitive molecular imaging," Nat. Med., vol. 13, pp. 95–99, 2007.

[6] Y. Kinemuchi, K. Ishizaka, H. Suematsu, W. Jiang, and K. Yatsui, "Magnetic properties of nanosize $NiFe_2O_4$ particles synthesized by pulsed wire discharge," Thin Solid Films, vol. 407, pp. 109–113, 2002.

[7] M. P. Reddy, R. A. Shakoor, A. M. A. Mohamed, M. Gupta, and Q. Huang, "Effect of sintering temperature on the structural and magnetic properties of $MgFe_2O_4$ ceramics prepared by spark plasma sintering," Ceram. Int., vol. 42, pp. 4221–4227, 2016.

[8] A. Goldman, Modern Ferrite Technology. New York, NY, USA: Springer Science + Business Media, 2006.

[9] G. Busca, E. Finocchio, V. Lorenzelli, M. Trombetta, and S. A. Rossini, "IR study of alkene allylic activation on magnesium ferrite and alumina catalysts," J. Chem. Soc., Faraday Trans., vol. 92, pp. 4687–4693, 1996.

[10] P. P. Hankare, S. D. Jadhav, U. B. Sankpal, R. P. Patil, R. Sasikala, and I. S. Mulla, "Gas sensing properties of magnesium ferrite prepared by co-precipitation method," J. Alloys Compd., vol. 488, pp. 270–272, 2009.

[11] Z. Hammache, A. Soukeur, S. Omeiri, B. Bellal, and M. Trari, "Physical and photo-electrochemical properties of $MgFe_2O_4$ prepared by sol–gel route: Application to the photodegradation of methylene blue," J. Mater. Sci.: Mater. Electron., vol. 30, pp. 5375–5382, 2019.

[12] Y. Watanabe et al., "Development of a second radiofrequency ablation using sintered $MgFe_2O_4$ needles and alternating magnetic field for human cancer therapy," Biomed. Mater. Eng., vol. 19, pp. 101–110, 2009.

[13] M. Pavlovic, C. Jovalekic, A. S. Nikolic, D. Manojlovic, and N. Sojic, "Mechanochemical synthesis of stoichiometric $MgFe_2O_4$ spinel," J. Mater. Sci., vol. 20, pp. 782–787, 2009.

[14] P. Holec, J. Plocek, D. Niznansky, and J. P. Vejpravova, "Preparation of $MgFe_2O_4$ nanoparticles by microemulsion method and their characterization," J. Sol–Gel Sci. Technol., vol. 51, pp. 301–305, 2009.

[15] P. P. Goswami, H. A. Choudhury, S. Chakma, and V. S. Moholkar, "Sonochemical synthesis and characterization of manganese ferrite nanoparticles," Ind. Eng. Chem. Res., vol. 52, pp. 17848–17855, 2013.

[16] S. J. Haralkar, R. H. Kadam, S. S. More, S. E. Shirsath, M. L. Mane, S. Patil, and D. R. Mane, "Substitutional effect of Cr^{3+} ions on the properties of Mg–Zn ferrite nanoparticles," Physica B: Condens. Matter, vol. 407, pp. 4338–4346, 2012.

[17] L. Zhao et al., "Studies on the magnetism of cobalt ferrite nanocrystals synthesized by hydrothermal method," J. Solid State Chem., vol. 18, pp. 245–252, 2008.

[18] R. Q. Chu and Z. J. Xu, "Synthesis of mixed-conducting oxide $SrFeCo_{0.5}O_{\gamma}$ powder by auto-combustion of citrate nitrate gel," J. Electroceram., vol. 21, pp. 778–781, 2008.

[19] S. Naz, S. K. Durrani, A. H. Qureshi, M. A. Hussain, and N. Hussain, "Nanosized bismuth titanate ($Bi_4Ti_3O_{12}$) system derived through auto-combustion process using suspension titania (TiO_2)," J. Therm. Anal. Calorim., vol. 114, pp. 719–723, 2013.

[20] S. Mahato and S. Banerjee, "Dielectric characteristics of $MgFe_2O_4$ ferrite prepared by sol–gel auto-combustion method," J. Mater. Today: Proc., vol. 4, pp. 5525–5531, 2017.

[21] Z. T. Khodair, N. M. Ibrahim, T. J. Kadhim, and A. M. Mohammad, "Synthesis and characterization of nickel oxide (NiO) nanoparticles using an environmentally friendly method and their biomedical applications," Chem. Phys. Lett., vol. 797, pp. 139564, 2022.

[22] Y. Jiang and A. Sun, "Effect of pH on the microstructure and magnetic properties of $Cu_{0.2}Co_{0.8}Fe_2O_4$ synthesized by sol–gel method," J. Sol–Gel Sci. Technol., vol. 109, pp. 773–783, 2024.

[23] N. Suo et al., "Preparation and study of lattice structure and magnetic properties of Bi^{3+} ion-doped Ni–Mg–Co ferrites by sol–gel auto-combustion method," J. Sol–Gel Sci. Technol., vol. 95, pp. 360–374, 2020.

[24] A. M. Mohammad, S. M. A. Ridha, and T. H. Mubarak, "Dielectric properties of Cr-substituted cobalt ferrite nanoparticles synthesized by citrate–gel auto-combustion method," Int. J. Appl. Eng. Res., vol. 13, pp. 6026–6035, 2018.

[25] A. M. Mohammad, H. Mehranfar, K. S. Rasol, M. M. Kareem, Y. H. Azeez, and M. M. Mohammed, "Temperature dependence of structural, morphological and magnetic properties of cobalt–cadmium ferrite nanoparticles: supported by theoretical study," Bull. Mater. Sci., vol. 47, p. 24, 2024.

[26] Ch. V. Reddy et al., "Investigation of structural, thermal and magnetic properties of cadmium substituted cobalt ferrite nanoparticles," Superlattices Microstruct., vol. 82, pp. 165–173, 2015.

[27] J. Bennet, R. Tholkappiyan, K. Vishista, N. V. Jaya, and F. Hamed, "Attestation in self-propagating combustion approach of spinel AFe_2O_4 (A = Co, Mg, and Mn) complexes bearing mixed oxidation states: magneto-structural properties," Appl. Surf. Sci., vol. 383, pp. 113–125, 2016.

[28] M. R. Barati, "Characterization and preparation of nanocrystalline MgCuZn ferrite powders synthesized by sol–gel auto-combustion method," J. Sol–Gel Sci. Technol., vol. 52, pp. 171–178, 2009.

[29] A. Mohammad, S. Aliridha, and T. Mubarak, "Structural and magnetic properties of Mg–Co ferrite nanoparticles," Dig. J. Nanomater. Biostruct., vol. 13, pp. 615–623, 2018.

[30] H. S. Ahmed, S. A. Hussen, and A. M. Mohammad, "Synthesis and characterization of $Zn_{0.8}Co_{0.2}Fe_2O_4$ ferrite nanoparticles: magnetic and structural insights," J. Sol–Gel Sci. Technol., vol. 115, pp. 17–29, 2025.

[31] R. Kumar, P. Barman, and R. R. Singh, "An innovative direct nonaqueous method for the development of Co-doped Ni–Zn ferrite nanoparticles," Mater. Today Commun., vol. 27, p. 102238, 2021.

[32] M. B. Jumaa, T. H. Mubarak, and A. M. Mohammad, "Exploring Cu-substituted Zn nanoferrites: synthesis, structural, magnetic, morphological, and antibacterial properties," J. Sol–Gel Sci. Technol., vol. 114, pp. 841–856, 2025.

[33] Sh. I. Hussein, A. S. Elkady, M. M. Rashad, A. G. Mostafa, and R. M. Megahid, "Structural and magnetic properties of magnesium ferrite nanoparticles prepared via EDTA-based sol–gel reaction," J. Magn. Magn. Mater., vol. 379, pp. 9–15, 2015.

[34] M. Beyranvand, A. Zahedi, and A. Gholizadeh, "Cadmium substitution effect on microstructure and magnetic properties of Mg–Cu–Zn ferrites," Front. Mater., vol. 8, pp. 779–837, 2022.

[35] A. R. Jdidi et al., "Enhancing dielectric properties of $CuFe_2O_4$ spinel ferrites through Mg, Co, and Cr doping: a sol–gel synthesis approach," J. Sol–Gel Sci. Technol., pp. 1–15, 2024.

[36] R. Irandoust and A. Gholizadeh, "A comparative study of the effect of the non-magnetic and magnetic trivalent rare-earth ion substitutions on bismuth ferrite properties: correlation between the crystal structure and physical properties," Solid State Sci., vol. 101, pp. 106–142, 2020.

[37] V. P. Senthil, J. Gajendiran, S. Gokul Raj, T. Shanmugavel, G. R. Kumar, and C. P. Reddy, "Study of structural and magnetic properties of cobalt ferrite ($CoFe_2O_4$) nanostructures," Chem. Phys. Lett., vol. 695, pp. 19–23, 2018.

[38] W. Meng, F. Li, D. G. Evans, and X. Duan, "Preparation of magnetic material containing $MgFe_2O_4$ spinel ferrite from a Mg–Fe(III) layered double hydroxide intercalated by hexacyanoferrate(III) ions," Mater. Chem. Phys., vol. 86, pp. 1–4, 2004.

[39] L. Rajadurai et al., "Effective removal of tetracycline hydrochloride under visible light using $Mg_{1-x}Co_xFe_2O_4$ (x = 0.0–0.5) nanoparticles," Mater. Sci. Eng. B, vol. 308, p. 117614, 2024.

[40] M. B. Jumaa, T. H. Mubarak, and A. M. Mohammad, "Synthesis and characterization of spinel ferrite $Co_{0.8}Fe_{2.2}O_4$ nanoparticle," J. Univ. Anbar Pure Sci. (JUAPS), vol. 15, pp. 74–82, 2021.

[41] K. R. Sanchez-Lievanos, J. L. Stair, and K. E. Knowles, "Cation distribution in spinel ferrite nanocrystals: characterization, impact on their physical properties, and opportunities for synthetic control," Inorg. Chem., vol. 60, pp. 4291–4305, 2021.

[42] M. G. Naseri, E. B. Saion, H. A. Ahangar, M. Hashim, and A. H. Shaari, "Synthesis and characterization of manganese ferrite nanoparticles by thermal treatment method," J. Magn. Magn. Mater., vol. 323, pp. 1745–1749, 2011.

[43] R. G. Kulkarni and H. H. Joshi, "Comparison of magnetic properties of $MgFe_2O_4$ prepared by wet-chemical and ceramic methods," J. Solid State Chem., vol. 64, pp. 141–147, 1986.

[44] S. M. M. Sangmanee and A. Wiengmoon, "Nanoscale research on ferrite materials," Nanoscale Res. Lett., vol. 4, p. 221, 2008.

[45] G. V. M. Jacintho, A. G. Brolo, P. Corio, P. A. Z. Suarez, and J. C. Rubim, "Structural investigation of MFe_2O_4 (M = Fe, Co) magnetic fluids," J. Phys. Chem. C, vol. 113, pp. 7684–7691, 2009.

[46] T. Şaşmaz Kuru, "Effect of calcination temperature on structural, magnetic, and dielectric properties of $Mg_{0.75}Zn_{0.25}Al_{0.2}Fe_{1.8}O_4$ ferrites," J. Mater. Sci.: Mater. Electron., vol. 35, p. 415, 2024.

[47] N. Kannapiran, A. Muthusamy, P. Chitra, S. Anand, and R. Jayaprakash, "Poly(o-phenylenediamine)/$NiCoFe_2O_4$ nanocomposites: synthesis, characterization, magnetic and dielectric properties," J. Magn. Magn. Mater., vol. 423, pp. 208–216, 2017.

[48] H. M. Abdallah, T. Moyo, and N. Ngema, "The effect of temperature on the structure and magnetic properties of $Co_{0.5}Ni_{0.5}Fe_2O_4$ spinel nanoferrite," J. Magn. Magn. Mater., vol. 394, pp. 223–228, 2015.

[49] B. Dash, K. L. Routray, S. Saha, P. Sarun, and S. Sarangi, "Insights into the effects of Mn substitution in $CoFe_2O_4$ nanoferrites involving high-frequency storage device applications," Int. J. Miner. Metall. Mater., vol. 32, pp. 1245–1258, 2025.

[50] S. Liu, G. Doyle, G. E. Kuhl, C. Chen, M. Walmer, and Y. Liu, "Temperature dependence of coercivity in Sm_2TM_{17} magnets and domain wall motion in magnetic materials," IEEE Trans. Magn., vol. 37, pp. 2521–2524, 2001.

[51] H. Sh. Ahmed, S. R. Saeed, and A. M. Mohammad, "Influence of calcination temperature on magnetic properties and antibacterial activities of Co–Ni–Cd–Fe_2O_4 nanocomposites," J. Supercond. Nov. Magn., vol. 38, p. 147, 2025.

[52] S. Divya et al., "Impact of Zn doping on the dielectric and magnetic properties of $CoFe_2O_4$ nanoparticles," Ceram. Int., vol. 48, pp. 33208–33218, 2022.